Influence of coil geometry, supply conditions and nanoparticle heating properties on magnetic hyperthermia in mouse models

International Journal of Thermal Sciences 203 (2024) 109151

Contents lists available at ScienceDirect

International Journal of Thermal Sciences

journal homepage: www.elsevier.com/locate/ijts

Influence of coil geometry, supply conditions and nanoparticle heating properties on magnetic hyperthermia in mouse models

Marta Vicentini *, Riccardo Ferrero, Alessandra Manzin **

Istituto Nazionale di Ricerca Metrologica (INRiM), Strada delle Cacce 91, 10135, Torino, Italy

ARTICLE INFO

Keywords:
Bioheat transfer model
Computational electromagnetism
Finite element method
In silico experiments
Magnetic field applicators
Magnetic hyperthermia
Magnetic nanoparticles
Mouse model
Numerical simulations
Thermal therapies

ABSTRACT

For *in vivo* magnetic hyperthermia tests, which are typically conducted on small animal models, one of the objectives is the design of alternating current (AC) magnetic field applicators able to guarantee an effective activation of magnetic nanoparticles (MNPs). During therapy application, it is critical to optimize heat deposition due to MNPs and minimize side effects in healthy tissues. For an accurate treatment planning, it is required to carefully select the geometry of the applicator coils and their location with respect to the body, as a function of the position and size of the tumour target region. Additionally, one should preliminary estimate the impact of experimental conditions on the MNP heating efficiency and thus on their capability to induce a temperature increase in tissues. Biophysical constraints have also to be taken into account in the choice of AC magnetic field parameters (frequency and amplitude), to avoid eddy current effects as much as possible.

In this study, we present realistic simulations of preclinical tests on a mouse model, evaluating thermal response under various experimental conditions. We investigate different field applicator configurations, including helical, Helmholtz and pancake coils, while also analysing the role of the amplitude and frequency of the supply current, as well as of the type and administered dose of MNPs. The temperature increase in tissues, resulting from the heating effects due to AC magnetic field exposure and MNP activation, is calculated by means of in-house finite element models that solve the low-frequency electromagnetic field problem and the bioheat transfer equation. This *in silico* approach, which is applicable to any type of field applicators and MNPs, has been demonstrated to provide useful insights for the optimization of *in vivo* experiments, enabling the design of safer and more effective treatments.

1. Introduction

Magnetic hyperthermia has shown great potential as an adjuvant to standard cancer therapies, such as radiotherapy or chemotherapy, due to its high biosafety, deep-tissue penetration, and selective tumour killing [1]. This treatment is based on the administration of magnetic nanoparticles (MNPs) within a target region, i.e. the diseased tissue, and on their activation with alternating current (AC) magnetic fields, with frequency between 50 kHz and 1 MHz [2]. The MNP activation leads to a local release of heat that produces an increase in temperature within the tumour, inducing cancer cell damage when average temperatures in the range of 40–45 °C are reached [3].

Preclinical tests on murine models (mice, rats) are commonly used to evaluate the therapeutic efficacy of magnetic hyperthermia [4,5]. One of the issues to be faced for *in vivo* treatments is the proper design of the setup for the generation of the AC magnetic field, in order to optimize heat deposition and minimize side effects in healthy tissues as much as possible. Several factors have to be taken into account, including (i) the fulfilment of biophysical constraints when selecting the AC magnetic field parameters (frequency f and peak amplitude $\hat{H}_a$), (ii) the dependence of the MNP heating efficiency on the experimental conditions, and (iii) the choice of the geometry of the field applicator and its placement with respect to the body.

In magnetic hyperthermia, biophysical constraints were introduced as limits on the magnetic field parameters, which enable us to guarantee safe heating conditions, without undesired eddy current effects associated with electromagnetic (EM) field exposure [6]. A first criterion, known as the Atkinson-Brezovich limit, was proposed in 1984, i.e. $\hat{H}_a \times f \leq 4.85 \bullet 10^8$ A/(m·s) [7], but in almost all the preclinical studies this was not satisfied [8–26]; a less restrictive limit was introduced by Hergt

* Corresponding author.
** Corresponding author.
E-mail addresses: m.vicentini@inrim.it (M. Vicentini), a.manzin@inrim.it (A. Manzin).

https://doi.org/10.1016/j.ijthermalsci.2024.109151
Received 15 December 2023; Received in revised form 11 April 2024; Accepted 10 May 2024
Available online 19 May 2024

and Dutz in 2007, i.e. $\hat{H}_a \times f \leq 5 \bullet 10^9$ A/(m·s) [27]. In recent *in silico* investigations on murine models, it was demonstrated that in 30 g mice the thermal effects due to the only EM field exposure are very weak, also when the Hergt-Dutz limit is overcome. However, significant temperature increases were found in 500 g rats, especially when the field is applied transversally to the body longitudinal axis [28].

Besides safety reasons, the selection of f and $\hat{H}_a$ should be carefully made also for assuring an adequate MNP heating efficiency. This can be quantified by means of the specific loss power (SLP), i.e. the power dissipated per unit mass of magnetic material, derived from calorimetric or thermometric measurements [29,30]. For a specific sample of MNPs, higher values of SLP can be obtained by increasing f and/or $\hat{H}_a$ [31–34], thus the magnetic field in the target region should be sufficiently large to enable the MNP activation [35].

Regarding the geometry of the field applicator, there are no currently available standards for the definition of the setups to be used *in vivo*. Anyway, there is a wide range of applicators suitable for preclinical tests of magnetic hyperthermia, comprising custom made as well as commercial setups specifically designed for research or dedicated for other purposes (e.g. induction welding), and then adapted. Different geometrical configurations were implemented and applied, including helical or Helmholtz coils with the animal positioned totally or partially inside [36,37], and helical or pancake coils placed in proximity to the animal body, close to the target region [38,39]. Strong efforts were also made to optimize the supply electronic circuits, in order to obtain versatile devices able to operate under a wide range of field frequencies and amplitudes [40,41], also exploiting non-sinusoidal waveforms [42,43]. Depending on the applicator geometrical configuration, size, position and supply conditions, variations are expected in the spatial distribution and magnitude of the magnetic field within the tumour, with a consequent impact on the heat release from the MNPs and thus on the temperature increase reached during hyperthermia sessions [44].

In this scenario, *in silico* tests are a valid tool for addressing the engineering of magnetic field applicators, their operating frequency and supply current, and their placement with respect to the body, as a function of the position of the target region within the body and of the heating properties of the used MNPs. In this paper, we perform realistic simulations of preclinical tests on a 30 g mouse, evaluating the thermal response under different experimental conditions. In particular, we consider various magnetic field applicators (with helical, pancake and Helmholtz-type geometry), varying the frequency and peak amplitude of the supply current, the type of MNPs, their administered dose and confinement. The analysis is performed by means of in-house finite element solvers [35,45], which enable us to evaluate the magnetic field spatial distribution within the target region, the thermal effects due to both MNP excitation and EM field exposure, under different conditions of magnetic field application.

The dependence of the MNP heating efficiency on the experimental conditions is modelled taking into account different aspects. These include the influence of the AC magnetic field parameters on the MNP heating properties (SLP), and the effects on temperature rise when the MNPs are dispersed in a target region with non-uniform magnetic field spatial distribution. The second aspect, which becomes important for particular coil applicator geometries and positions, is handled by introducing a locally variable MNP heating power, while in most of the previous studies the field is supposed to be uniform in the target region where the MNPs are dispersed.

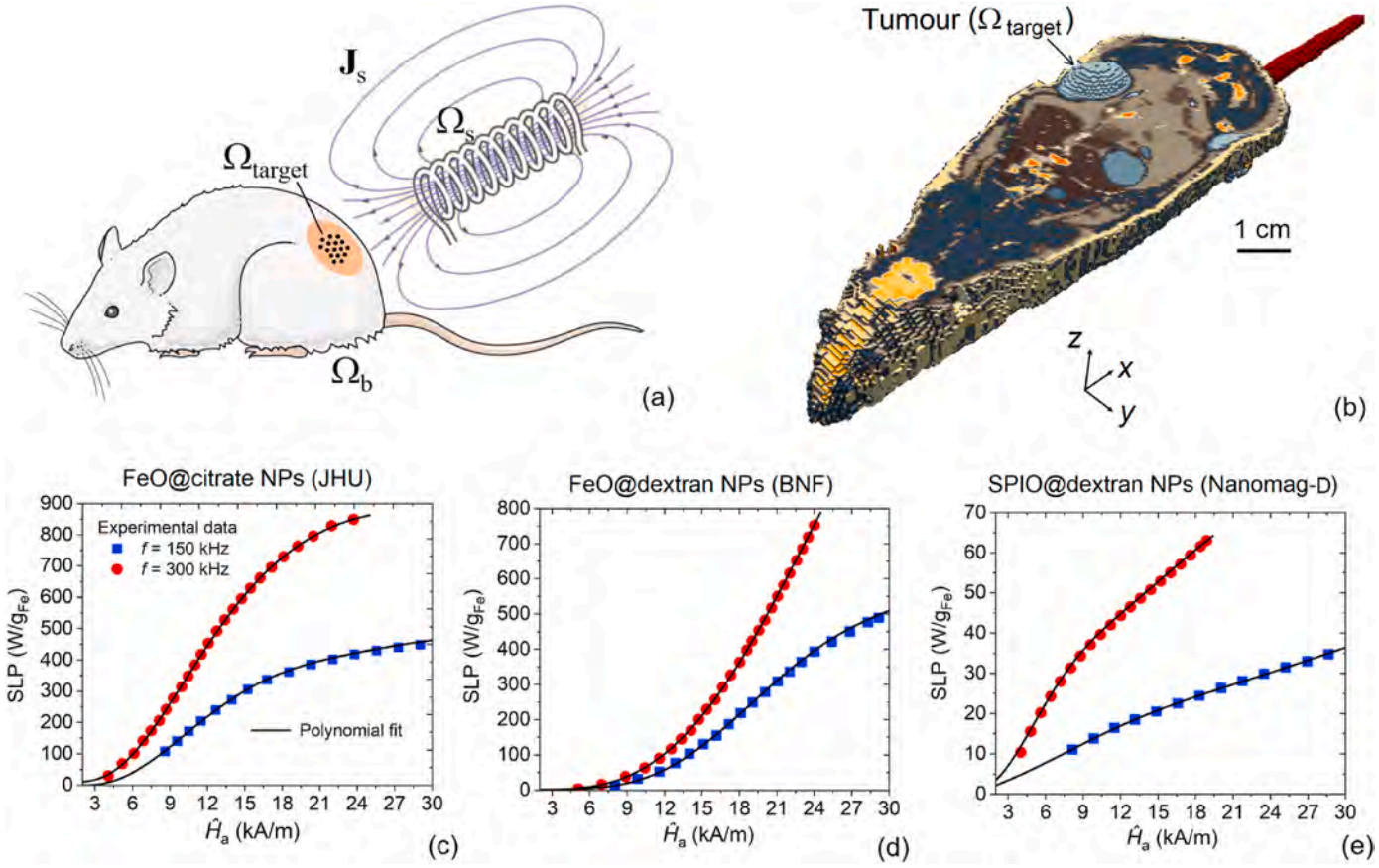

Fig. 1. (a) Schematic of an *in vivo* magnetic hyperthermia experiment, where a mouse is exposed to an AC magnetic field. The animal, defined by domain Ω_b, presents a tumour region, Ω_{target}, where MNPs are distributed. The field applicator is represented by a solenoid Ω_s with current density vector $\mathbf{J}_s$. (b) Portion of the digital phantom of the considered mouse model. Specific loss power (SLP) versus AC magnetic field peak amplitude for (c) FeO@citrate (JHU) NPs, (d) FeO@dextran (BNF) NPs, and (e) SPIO@dextran (Nanomag-D) NPs. The blue and red markers correspond to the experimental data extrapolated from the literature for the frequencies of 150 and 300 kHz [33], respectively, whereas the black curves to their polynomial interpolation.

2. Numerical model

The study is carried out by means of in-house numerical models for the calculation of (i) the magnetic field produced by the applicator, (ii) the induction phenomena due to EM field exposure, and (iii) the thermal effects consequent to the AC magnetic field application and MNP activation. Fig. 1a schematizes the 3D domain under analysis, comprising the applicator coil (Ω_s) and the animal body (Ω_b), with the indication of the target region or tumour to be treated (Ω_{target}).

2.1. Calculation of magnetic field within the body

The spatial distribution of the magnetic field produced by the applicator in the body region Ω_b is calculated in two steps. First, we determine the spatial distribution of the current density vector $\mathbf{J}_s$ within the applicator coil Ω_s, by solving the current-field equation with finite element method (FEM), using linear basis functions and discretization with tetrahedrons of Ω_s. We implement the model by considering current-driven formulation [46] and quasi-static conditions. Second, we calculate the magnetic field in the body, as:

$$\mathbf{H}_s(\mathbf{r}_b) = \frac{1}{4\pi}\int_{\Omega_s} \frac{\mathbf{J}_s(\mathbf{r}_s)\times(\mathbf{r}_b-\mathbf{r}_s)}{|\mathbf{r}_b-\mathbf{r}_s|^3} dv_s \tag{1}$$

where $\mathbf{r}_s$ indicates the vector position of a point inside the source conductors and $\mathbf{r}_b$ the vector position of a point in Ω_b. Moreover, we evaluate the corresponding magnetic vector potential $\mathbf{A}_s$, as:

$$\mathbf{A}_s(\mathbf{r}_b) = \frac{\mu_b}{4\pi}\int_{\Omega_s} \frac{\mathbf{J}_s(\mathbf{r}_s)}{|\mathbf{r}_b-\mathbf{r}_s|} dv_s, \tag{2}$$

where μ_b is the body magnetic permeability, assumed to be equal to the one of vacuum.

2.2. Calculation of induction phenomena within the body

The induction phenomena produced in the body during the application of the AC magnetic field are evaluated disregarding displacement currents. By assuming that the magnetic field produced by the applicator is not appreciably modified by the eddy currents induced in the body, we can express the current density vector $\mathbf{J}_b$ inside Ω_b as

$$\mathbf{J}_b = \sigma\mathbf{E}_b = -\sigma(\nabla\phi + j2\pi f\mathbf{A}_s), \tag{3}$$

where $\mathbf{E}_b$ is the electric field vector, j is the imaginary unit, σ is the tissue electrical conductivity, ϕ is the electric scalar potential and $\mathbf{A}_s$ is calculated according to (2) [47]. Considering the charge conservation equation $\nabla\cdot\mathbf{J}_b = 0$ and the boundary condition $\mathbf{J}_b\cdot\mathbf{n} = 0$ (with $\mathbf{n}$ being the unit vector normal to $\partial\Omega_b$), we derive the following equation:

$$\int_{\Omega_b} \sigma\nabla\phi\cdot\nabla w dv_b = -j2\pi f\int_{\Omega_b} \sigma\mathbf{A}_s\cdot\nabla w dv_b, \tag{4}$$

after applying the weak formulation with test function w. Also (4) is solved with FEM, using linear basis functions and discretization with tetrahedrons of Ω_b, after subdividing into 6 tetrahedrons each voxel of the body digital phantom.

2.3. Calculation of thermal effects within the body

The thermal effects within Ω_b, consequent to the AC magnetic field application and MNP activation, are evaluated by solving the Pennes' bioheat transfer equation with FEM, using the same discretization with tetrahedrons adopted for the calculation of induction phenomena. The application of the weak formulation with test function w leads to the following equation:

$$\begin{aligned}\int_{\Omega_b} \rho C_p\frac{\partial T}{\partial t} w dv_b = &-\int_{\Omega_b} k\nabla T\cdot\nabla w dv_b + \int_{\partial\Omega_b} k\frac{\partial T}{\partial n} w ds_b \\ &-\int_{\Omega_b} WC_{blood} T w dv_b + \int_{\Omega_b} WC_{blood} T_{blood} w dv_b \\ &+\int_{\Omega_b} Q_m w dv_b + \int_{\Omega_b} Q_{EM} w dv_b + \int_{\Omega_{target}} Q_{MNPs} w dv_{target},\end{aligned} \tag{5}$$

where T is the tissue temperature, ρ is the tissue density, C_p is the tissue heat capacity, k is the tissue thermal conductivity, Q_m is the tissue specific metabolic heat generation rate, W is the tissue-blood perfusion rate, C_{blood} is the blood heat capacity and T_{blood} is the arterial temperature. C_{blood} and T_{blood} are fixed to 3617 J/(K·kg) and 37 °C, respectively. Q_{EM} is the specific heating power produced by the AC magnetic field, obtained with the low-frequency EM field solver described in Subsection 2.2, as $Q_{EM} = \sigma|\mathbf{E}_b|^2/2$. Q_{MNPs} is the specific heating power released by the MNPs, and it is expressed as the product of the SLP and the dose of the administered MNPs.

In the presence of a non-uniform magnetic field spatial distribution in the target region, as occurs for many applicator configurations, Q_{MNPs} varies locally, and results to be a function of the local value of the field peak amplitude $\hat{H}_a(\mathbf{r})$. Once known the dependence of the SLP values on the magnetic field parameters (e.g. from experimental or modelling estimation), we can derive the expression of Q_{MNPs} for a specific supply frequency, as follows:

$$Q_{MNPs}(\mathbf{r}) = dose_{MNPs}(\mathbf{r})\cdot SLP[\hat{H}_a(\mathbf{r})] = dose_{MNPs}(\mathbf{r})\cdot\sum_{p=0}^{P}\left[a_p\hat{H}_a^p(\mathbf{r})\right], \tag{6}$$

where the SLP is approximated as a polynomial function of $\hat{H}_a$, with degree P and coefficients a_p, obtained by interpolating the measured or calculated curve versus $\hat{H}_a$. The dose of the MNPs, assumed to be uniformly distributed within the target region Ω_{target} (if not differently specified) is quantified as the mass concentration of iron [Fe].

Equation (5) is completed by the following boundary condition at the interface $\partial\Omega_b$ between the skin and the surrounding environment:

$$q = -k\frac{\partial T}{\partial n} = -h(T_{ext} - T_{skin}), \tag{7}$$

where q is the outward heat flux, T_{ext} is the external temperature (set at 25 °C), T_{skin} is the skin temperature and h is the heat transfer coefficient.

The time evolution of the temperature during the heating and successive cooling transients is calculated by time-integrating (5) with the Crank-Nicolson's method, fixing the temperature at the initial time instant to the baseline temperature. The thermal equilibrium configuration is directly calculated by solving the steady-state version of (5).

3. Simulation parameters

To mimic preclinical tests of magnetic hyperthermia, we consider a voxel-based mouse model, obtained by resizing the Sprague Dawley rat, available on the IT'IS Foundation database [48], by a scaling factor of 2.6. The resulting animal, which has a body length of about 8.7 cm, presents a large tumour on the flank, with a size of 815 mm^3 (see Fig. 1b) and is discretized with 0.38 mm sized voxels, in turn subdivided into 6 tetrahedrons. Except for the tumour region that represents the target region Ω_{target}, the tissue properties (electrical conductivity σ, density ρ, heat capacity C_p, thermal conductivity k, perfusion rate W and specific metabolic heat generation rate Q_m) are retrieved from the IT'IS Foundation database [49] (see the Supplemental Material where they are listed in Table S1). For Ω_{target}, we fix σ to 0.8 S/m [50], ρ to 1045 kg/m^3, C_p to 3760 J/(K·kg), k to 0.51 W/(K·m), W to 9.97 kg/(s·m^3) and Q_m to 31.87 kW/m^3 [51]. To replicate a condition in which free convection prevails, the heat transfer coefficient h is set at 3.5 W/(m^2·K) [50].

We simulate different experimental conditions by varying the geometry of the magnetic field applicator, the supply current peak amplitude and frequency, and the type of MNPs, assumed to be uniformly distributed within Ω_{target}, if not differently specified. This is generally a valid condition for multi-injection administration. The considered applicators comprise: (i) an 8-turn helical coil with an outer diameter of 5 cm; (ii) a 3-turn pancake coil with an outer diameter of 4.75 cm; (iii) a Helmholtz-type coil with 3 turns per side and an outer diameter of 7.85 cm. The coil geometries and dimensions refer to custom-made or commercial applicators already employed *in vivo* studies [8,36–39,52].

The positions of the coils with respect to the animal body are defined with the aim of focusing the magnetic field as much as possible in the target region and mimicking experimental conditions typically adopted in preclinical tests. Fig. 2 illustrates the selected setups: for the 8-turn coil we have two configurations, in the first one (configuration #1),

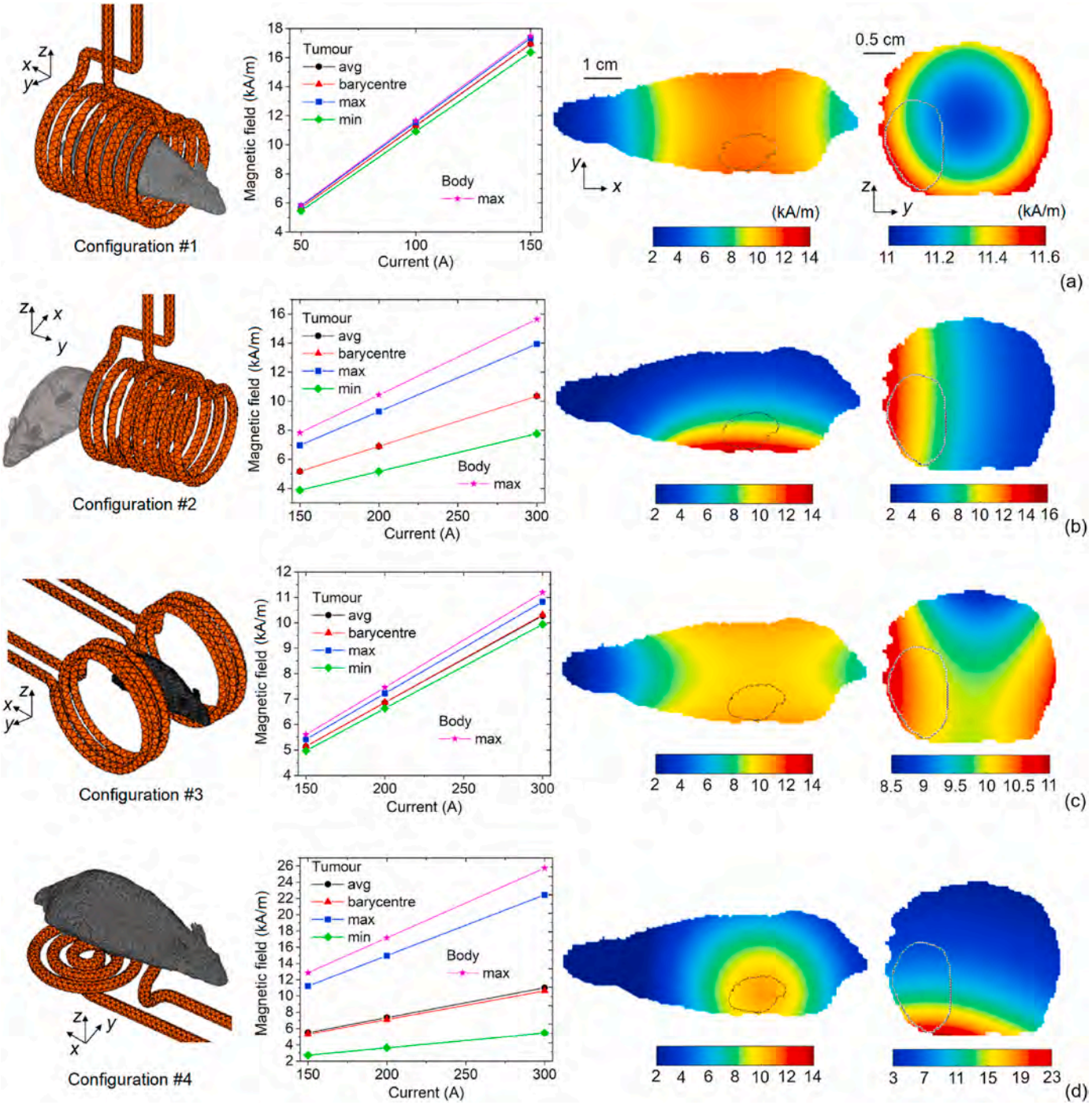

Fig. 2. Analysis of magnetic field generated in the mouse body for (a) configuration #1: 8-turn coil with mouse placed inside, (b) configuration #2: 8-turn coil with mouse placed outside, (c) configuration #3: Helmholtz coil, and (d) configuration #4: pancake coil. Left: schematics of the four applicator-mouse configurations. Middle: average, maximum and minimum magnetic field peak amplitude in the tumour region versus supply current (the field at the tumour barycentre and the maximum value in the body are also reported). Right: maps of the magnetic field peak amplitude over a longitudinal and a transversal section of the mouse, crossing the tumour barycentre, calculated by supplying the applicator in configuration #1 with a current of 100 A and the applicators in the other configurations with a current of 300 A.

the mouse body is placed inside apart from the head (Fig. 2a, left), in the second one (configuration #2), the mouse is placed outside with the coil positioned in close proximity to the tumour (Fig. 2b, left); for the Helmholtz coil (configuration #3), the mouse is located between the two wires, closer to one side (Fig. 2c, left); for the pancake coil (configuration #4), the mouse is positioned above the coil (Fig. 2d, left), similarly to the experimental condition found in Ref. [52]. The supply current peak amplitude $\hat{I}$ is varied in a range that depends on the considered setup (from 50 to 150 A for the 8-turn coil with the mouse inside, and from 150 to 300 A for the other applicator-mouse configurations). The selected values are in line with previous preclinical studies adopting custom-made applicators, where supply currents with peak amplitudes from 70 A [8] to more than 400 A [36,39] are used. Lower currents are chosen for configuration #1, being sufficient for reaching magnetic field amplitudes needed for activating the MNPs, while with the other configurations higher currents have to be supplied.

The three types of MNPs considered in the analysis refer to iron oxide based materials whose relevant properties are available from the literature in terms of SLP versus magnetic field peak amplitude $\hat{H}_a$ and frequency f [33]. Specifically, these are: (1) core-shell NPs with citrate shell, from NanoMaterials Technology Pte Ltd, commercialized as Johns Hopkins University (JHU) NPs [53]; (2) core-shell NPs with dextran shell, from micromod Partikeltechnologie GmbH, commercialized as bionized nanoferrite (BNF) NPs [54]; (3) matrix-based NPs constituted by superparamagnetic iron oxide (SPIO) NPs dispersed in a dextran matrix, from micromod Partikeltechnologie GmbH, commercialized as Nanomag-D NPs [52]. For simplicity, we refer to them as (1) FeO@citrate NPs, (2) FeO@dextran NPs and (3) SPIO@dextran NPs, respectively. The values of the SLP are extrapolated for two frequencies, i.e. 150 kHz and 300 kHz, fitting and extending the data from Ref. [33] down to very low fields.

4. Results and discussion

The modelling approach described in Section 2 is here applied to investigate the following aspects.

(i) the spatial distribution and amplitude of the magnetic field in the target region (tumour), as a function of the setup configuration (coil geometry and position with respect to the mouse body) and supply current;
(ii) the eddy current effects associated with the only EM field exposure and the possible occurrence of non-selective heating of healthy tissues;
(iii) the heating effects produced in the tumour after MNP excitation, as a function of MNP type, concentration and local distribution, setup configuration and supply current parameters (frequency and peak amplitude);
(iv) the time duration needed to reach thermal equilibrium.

4.1. Analysis of magnetic field exposure

In this sub-section, we compare the applicators in terms of the spatial distribution of the produced magnetic field as well as of the possible thermal effects, caused by eddy current generation. With the supply conditions reported in Section 3, the peak amplitude of the magnetic field applied at the tumour barycentre varies within the ranges 5.8−17 kA/m for configuration #1, 5.2−10.3 kA/m for configuration #2, 5.2−10.4 kA/m for configuration #3, and 5.3−10.6 kA/m for configuration #4 (Fig. 2, middle). Similar intervals of variation are also found for the average values, evaluated within the tumour.

The spatial distributions of the magnetic field produced by the applicators within the animal body are compared in the right part of Fig. 2, on both a longitudinal and a transversal cross section intersecting the tumour barycentre; in order to obtain similar values at the tumour barycentre a current of 100 A is used for configuration #1, while a current of 300 A is employed for the other configurations. Apart from configuration #1 (Fig. 2a), for which the magnetic field is practically uniform in overall the animal body, reaching a value around 11 kA/m, a great uniformity is also found with the Helmholtz-type coil in configuration #3 (Fig. 2c). In this case, the magnetic field in the tumour varies between 10 and 11 kA/m. In contrast, with the other two configurations there is a rapid decay of the magnetic field amplitude as the distance from the coil increases; in particular, for the 8-turn coil with the animal outside (configuration #2), the magnetic field in the tumour varies between 8 and 14 kA/m (Fig. 2b), while for the pancake coil (configuration #4), an even wider change is found, with the field ranging from 5.5 to 22.5 kA/m (Fig. 2d). This behaviour is reflected in the field-current plots (Fig. 2, middle), where the curves corresponding to the average, maximum and minimum magnetic field peak amplitudes in the tumour region are very close for configurations #1 and #3, corresponding to a uniform field, and spread out for configurations #2 and #4, indicating a strong heterogeneity.

With the selected interval of parameters for the supply current (frequency and peak amplitude), we can ensure compliance with the Hergt-Dutz limit for most of the considered cases. In particular, the limit is slightly overcome for configuration #1, when $f = 300$ kHz and $\hat{I} = 150$ A, with magnetic field peak values observed on the abdomen, flank and back surfaces, and for configuration #4, when $f = 300$ kHz and $\hat{I} = 200$ and 300 A, with magnetic field peak values on the abdomen. The thermal effects due to the only AC magnetic field exposure are illustrated in Fig. 3, which shows for all the configurations, as a function of the peak amplitude of the magnetic field averaged in the tumour region, the maximum temperature T_{max} and the average temperature T_{avg} inside the tumour, plus the maximum temperature external to the tumour $T_{max,ext}$, to investigate possible eddy current effects generated in healthy tissues. For each value of the average magnetic field reported in abscissa, the corresponding supply current can be derived from the graphs of Fig. 2, middle. The analysis is performed for f equal to 150 kHz and 300 kHz.

It can be noticed that the magnetic field exposure weakly affects the tumour temperature when $f = 150$ kHz, in this case the maximum increment in T_{avg}, in the order of 0.13 °C, is observed for configuration #1 when the average magnetic field is 17 kA/m ($\hat{I} = 150$ A). Anyway, T_{max} and $T_{max,ext}$ result to be lower than 37.3 °C. When $f = 300$ kHz, the maximum increment in T_{avg} is more significant, being 0.53 °C for configuration #1 and around 0.3 °C for configurations #2 and #3, while negligible variations are found for configuration #4. Also for the highest frequency, T_{max} and $T_{max,ext}$ result to be within safe limits, being well below 38 °C.

The thermal effects due to magnetic field exposure are clearly illustrated by the longitudinal maps in Fig. 3e, which reports the spatial distributions of the temperature at equilibrium, comparing the conditions corresponding to the different applicator-mouse configurations with the case of only metabolic heat present. The results with the field switched on are obtained having fixed f to 300 kHz and $\hat{I}$ to 300 A, apart from configuration #1, for which $\hat{I} = 100$ A, to compare conditions where similar field levels are reached. It is interesting to note that configurations #1, #2 and #4 lead to a similar temperature spatial distribution, with peak values in the tumour and in the surrounding regions, being characterized by the higher specific metabolic heat generation rate and interested by the stronger eddy current generation (the tumour is indeed located at one flank, where the transversal section is wider). Conversely, for configuration #3, the temperature increases approximately in the whole body; the reason is that the magnetic field is applied orthogonally to the mouse longitudinal axis, and thus the cross section where eddy currents appear interests practically all the animal, from tail to head. In this case, the maximum temperature increments, resulting in the order of 2 °C, are found in correspondence to muscle tissue near neck region.

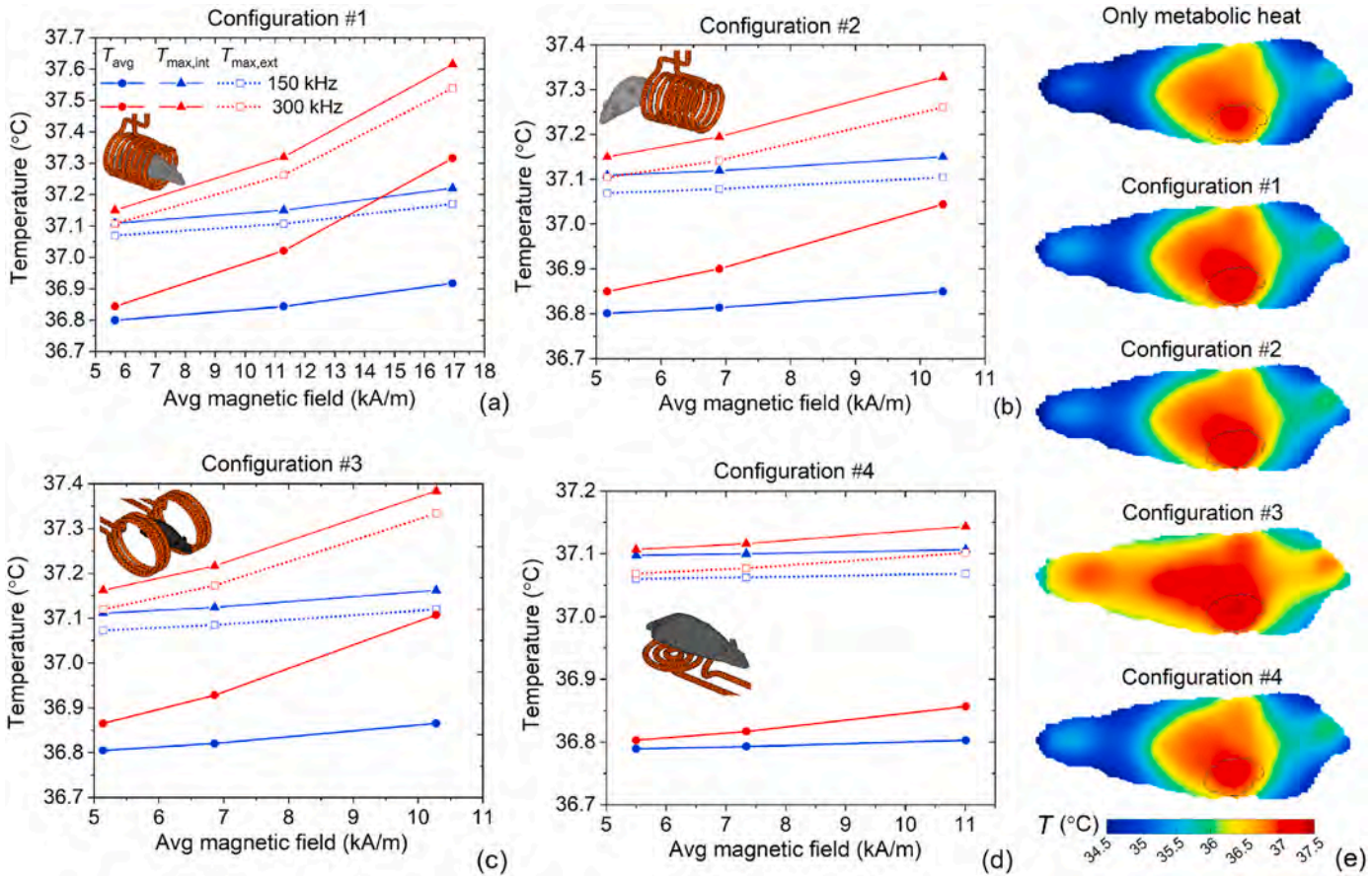

Fig. 3. Analysis of thermal effects due to AC magnetic field exposure for (a) configuration #1, (b) configuration #2, (c) configuration #3, and (d) configuration #4. The graphs show the maximum and average temperatures evaluated at thermal equilibrium within the tumour as a function of the average magnetic field in the tumour, for f equal to 150 kHz and 300 kHz (the maximum temperature external to the body is also reported). (e) Temperature maps calculated at thermal equilibrium across the mouse longitudinal section, comparing the heating contribution due to only metabolic heat (top) to the heating contribution of the AC magnetic field for the different configurations. The temperature spatial distributions are obtained by supplying the applicator in configuration #1 with a current of 100 A and the applicators in the other configurations with a current of 300 A, fixing f to 300 kHz.

4.2. Analysis of magnetic nanoparticle heating efficiency

In this sub-section, we compare the applicators in terms of the heating effects produced in the tumour by the AC magnetic field application and MNP activation. In particular, we analyse how the thermal effects can be tuned by varying the type of MNPs, their concentration, the setup configuration and the supply current parameters.

The combined action of magnetic field exposure and MNP excitation is first shown for FeO@citrate NPs in Fig. 4, which reports for all the configurations the maximum temperature T_{max} and the average temperature T_{avg} inside the tumour, plus the maximum temperature external to the tumour $T_{max,ext}$, as a function of the peak amplitude of the magnetic field averaged in the target region, for f equal to 150 kHz and 300 kHz. The results are obtained for an MNP dose corresponding to an iron mass concentration [Fe] of 1.25 mg/cm^3 within the tumour, which has been previously demonstrated to guarantee the achievement of therapeutic conditions (40−45 °C for T_{avg}), while fulfilling the Hergt-Dutz limit and under the assumption of magnetic field uniformly applied along the mouse longitudinal axis [35]. In particular, for the small animal here considered this condition corresponds to an average temperature increase from 3 up to 8 °C.

With configuration #1 (Fig. 4a), a current of 100 A, leading to an average magnetic field of 11 kA/m, is sufficient for achieving the therapeutic temperature range with $f = 150$ kHz, while with a 50 A current no significant differences are found in comparison to the case without MNPs, being the generated field too low to activate the MNPs. When supplying the applicator with a current of 150 A, corresponding to a field in the order of 17 kA/m, the upper limit of 45 °C is reached; a possible issue is that such temperature is also observed in the healthy tissues surrounding the tumour. When $f = 300$ kHz, smaller currents should be used to avoid the exceeding of the upper threshold temperature, i.e. currents around 75 A, leading to 8.5 kA/m average magnetic fields, could be optimal. On the contrary, with currents higher than 100 A, adverse thermal effects can occur (e.g., when $\hat{I} = 150$ A an average temperature of 50 °C is found in the tumour, corresponding to an average temperature increase of about 13 °C).

With the other configurations, higher currents have to be used to reach magnetic fields able to activate the MNPs. With configuration #2 (Fig. 4b), when $f = 150$ kHz, the maximum considered current (300 A) enables to obtain a 10.5 kA/m average field and thus only an average temperature of 40 °C in the tumour. With currents around 200 A, temperatures well below the therapeutic range are reached. When $f = 300$ kHz, currents in the order of 260 A should be selected to supply the applicator, in order to reach 9 kA/m average magnetic fields in the tumour, thus enabling the achievement of temperatures within the therapeutic range. With configuration #3 (Fig. 4c), a similar behaviour is found, in terms of supply conditions to be chosen to guarantee an effective magnetic hyperthermia application. With configuration #4 (Fig. 4d), when using the same current amplitudes, slightly larger average temperatures are obtained with respect to configurations #2 and #3, but the maximum temperatures (both in the tumour and in the external surrounding regions) are at least 1 °C greater, due to the strong

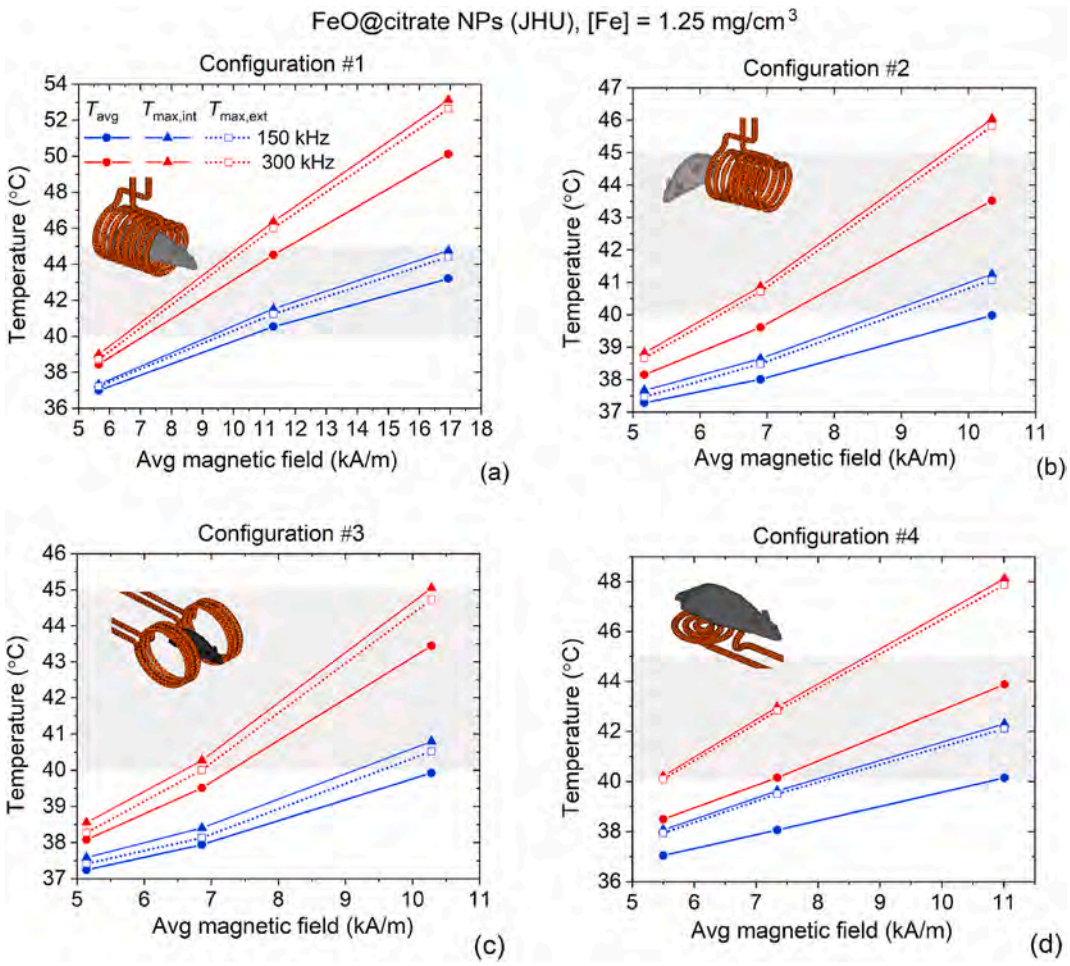

Fig. 4. Analysis of thermal effects due to FeO@citrate NP activation for (a) configuration #1, (b) configuration #2, (c) configuration #3, and (d) configuration #4. The graphs show the maximum and average temperatures evaluated at thermal equilibrium within the tumour as a function of the average magnetic field in the tumour, for f equal to 150 kHz and 300 kHz (the maximum temperature external to the body is also reported). The dose of the FeO@citrate NPs, assumed to be uniformly distributed within the tumour, corresponds to an iron mass concentration [Fe] of 1.25 mg/cm^3. The target temperature range for T_{avg} (40−45 °C) is indicated with the grey rectangle.

heterogeneity of the field, characterized by a discrepancy of about 100% between the maximum and average values (see Fig. 2d, middle).

To provide indications on the hyperthermia session duration, we calculate the time evolution of the maximum temperature T_{max} and the average temperature T_{avg} inside the tumour, during the heating and successive cooling transients. As an example, Fig. 5 reports the results obtained for FeO@citrate NPs with [Fe] = 1.25 mg/cm^3, having set the magnetic field frequency at both 150 and 300 kHz. It is important to note that the thermal equilibrium can be approached in about 5 min and fully achieved in 30 min, a time interval compatible with *in vivo* applications [8,36–39]. These features are characteristic of all the investigated cases, having fixed all the tissue properties.

The applicator performances are also investigated by considering a larger dose of FeO@citrate NPs, corresponding to an iron mass concentration [Fe] of 2 mg/cm^3 within the tumour; the relative results for the equilibrium condition are reported in Fig. 6. In this case, lower currents are adequate for reaching the therapeutic range, e.g. with configuration #1 (Fig. 6a) currents of 75 and 55 A are sufficient to arrive at 40 °C when f is equal to 150 and 300 kHz, respectively. However, major attention has to be paid to avoid the overcoming of the upper limit of 45 °C, which can be locally exceeded when the average applied field is only 8 kA/m (i.e., for a supply current around 70 A). With configurations #2 (Fig. 6b) and #3 (Fig. 6c), when f = 150 kHz, the larger MNP concentration enables to reach the therapeutic range with wider average field ranges, starting from approximately 8.5 kA/m, achievable with a current of about 250 A. When f = 300 kHz, fields in the order of 7 kA/m (obtainable with 200 A currents) allow to operate under target conditions. With configuration #4 (Fig. 6d), very careful attention has to be paid when selecting the supply current if f = 300 kHz, since in this case fields of 6.5 kA/m (and thus currents around 180 A) are enough large to exceed the therapeutic range, in terms of maximum temperatures reached in both the tumour and external surrounding regions.

As a comparison of the performances of the different applicators, Fig. 7 shows the spatial distributions of the temperature obtained at equilibrium on a transversal section crossing the tumour barycentre. The maps are calculated for all the applicator-mouse configurations, supplying the applicator in configuration #1 with a current of 100 A and the applicators in the other configurations with a current of 300 A, and fixing the frequency to 150 kHz. Different spatial distributions of FeO@citrate NPs are considered. In Fig. 7a the MNPs are assumed to be uniformly dispersed in the whole tumour with a dose corresponding to an iron mass concentration [Fe] of 2 mg/cm^3. For all configurations, the temperature increment is mainly concentrated within the tumour as a proof of the effective magnetic hyperthermia application, but with a different spatial distribution depending on the magnetic field focusing (see Fig. 2). The most heterogeneous distribution is observed with configuration #4, with temperature values varying between 38.6 °C and 45.6 °C in the entire tumour volume (the peaks are localized in the lower part adjacent to skin areas). In contrast, the temperature spatial distribution is more uniform with the other applicator-mouse configurations,

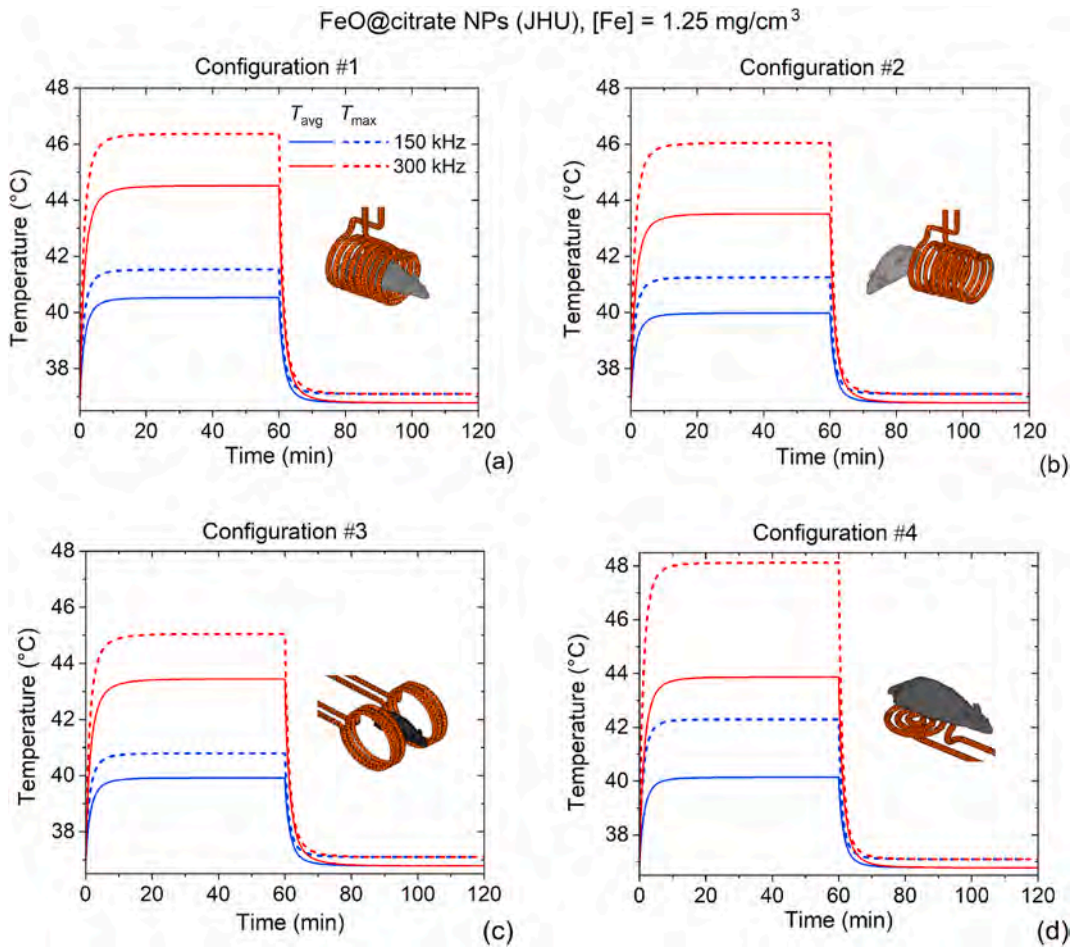

Fig. 5. Analysis of thermal effects due to FeO@citrate (JHU) NP activation for (a) configuration #1, (b) configuration #2, (c) configuration #3, and (d) configuration #4. The graphs show the time evolutions of the maximum and average temperatures within the tumour during the heating and cooling transients. The calculations are performed for f equal to 150 kHz and 300 kHz, switching off the magnetic field after 60 min. The dose of the FeO@citrate NPs, assumed to be uniformly distributed within the tumour, corresponds to an iron mass concentration [Fe] of 1.25 mg/cm^3.

especially for configuration #1, where the temperature varies in the range 42–44 °C in overall the tumour volume, reducing to 39.3 °C towards the internal tumour periphery. With configurations #2 and #3 the increments are more focused on the tumour side where the distance from the applicator wires is shorter, with tumour temperatures varying between 38.4 and 43.9 °C for configuration #2 and between 38.7 and 43.1 °C for configuration #3.

Although for all the applicator-mouse configurations the selected parameters enable to operate within the therapeutic range (apart from configuration #4 that leads to a slight exceeding of 45 °C), it is possible to observe that the tissues exhibiting temperatures higher than 40 °C extend significantly beyond tumour boundaries. Such effects appear not only in regions near the skin and thus closer to the applicator wires, but also within internal parts of the body. This can be quantified by evaluating the tissue volume outside the tumour, where the temperature exceeds 40 °C, as a percentage of the tumour volume itself. Such quantity varies from 49% with configurations #2 and #3 to 80% for configuration #1, while for configuration #4 a percentage in the order of 55% is found. Therefore, with a more uniform magnetic field distribution throughout the tumour region, as obtained with configuration #1, thermal effects can largely extend to the surrounding healthy tissues.

To reduce non-selective heating, one possibility is the dispersion of MNPs in a limited portion of the tumour, mimicking the administration with a single injection. As an example, Fig. 7b reports the results obtained by uniformly distributing the FeO@citrate NPs in a 4 mm diameter sphere centred in the tumour barycentre, with [Fe] fixed to 10 mg/cm^3. Small differences are found among the temperature maps, by varying the setup configuration, being comparable the magnetic field amplitude at the tumour barycentre. However, in this case the increase in temperature is strongly limited (occurring in a 5 mm sized region) and reaching a maximum temperature in the order of 43 °C, even if the dose of MNPs is incremented of five times. More evident differences among the set-up configurations can be appreciated when the MNPs are distributed within a region closer to the skin, due to the diverse magnetic field patterns, as shown in Fig. 2. As a proof, Fig. 7c illustrates the results obtained when the FeO@citrate NPs are uniformly distributed in a 4 mm diameter sphere located in the tumour and centred at about 2.6 mm from the skin, with [Fe] fixed to 10 mg/cm^3. In this case, the highest temperatures are obtained with configuration #4, reaching values higher than 45 °C.

Magnetic hyperthermia outcomes are strongly dependent on the type of used MNPs and their heating properties. This is well highlighted by the comparison of Figs. 4 and 8, the latter reports the results obtained when injecting in the tumour FeO@dextran NPs, whose SLP values are significantly lower than the ones of FeO@citrate NPs, within the interval of variation of the magnetic field generated by the applicators considered in this study. In particular, for the same iron mass concentration [Fe], when using FeO@dextran NPs much lower temperatures are reached, even below 40 °C, as happens for configurations #2 (Fig. 8b) and #3 (Fig. 8c) for both 150 and 300 kHz. With these applicator-mouse configurations, the maximum average magnetic field observable in the tumour is indeed around 10.5 kA/m (Fig. 2b and c), corresponding to an

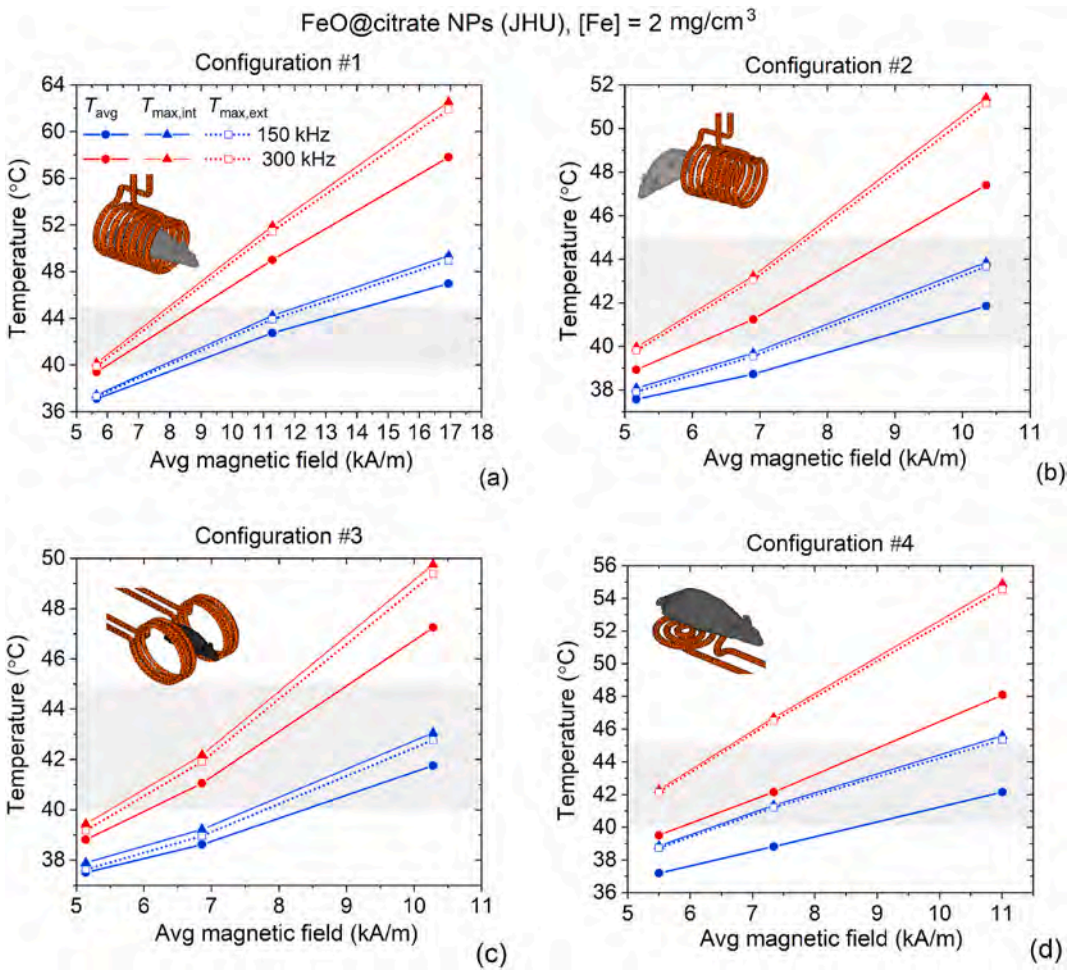

Fig. 6. Analysis of thermal effects due to FeO@citrate (JHU) NP activation for (a) configuration #1, (b) configuration #2, (c) configuration #3, and (d) configuration #4. The graphs show the maximum and average temperatures evaluated at thermal equilibrium within the tumour as a function of the average magnetic field in the tumour, for f equal to 150 kHz and 300 kHz (the maximum temperature external to the body is also reported). The dose of the FeO@citrate NPs, assumed to be uniformly distributed within the tumour, corresponds to an iron mass concentration [Fe] of 2 mg/cm^3. The target temperature range for T_{avg} (40−45 °C) is indicated with the grey rectangle.

SLP of 35 W/g_{Fe} (f = 150 kHz) and 67 W/g_{Fe} (f = 300 kHz) for FeO@-dextran NPs (Fig. 1d), against values of 170 and 360 W/g_{Fe} for FeO@-citrate NPs (Fig. 1c). Slightly larger temperatures are obtained with configuration #4 (Fig. 8d), being the maximum magnetic fields in the tumour doubled with respect to the previous configurations, anyway the therapeutic range is reached in terms of maximum temperature only when $\hat{I}$ = 300 A and f = 300 kHz, conditions for which the average temperature in the tumour is only 39 °C. On the contrary, with configuration #1 (Fig. 8a), it is possible to overcome 40 °C also in terms of average temperature values, but currents higher than 110 A (f = 150 kHz) and 140 A (f = 300 kHz) are needed.

Finally, we analyse what happens when considering widely used commercial MNPs, like SPIO@dextran (Nanomag-D) NPs, which are characterized by very low SLP values within the interval of variation of the magnetic field generated by the applicators considered in this study (Fig. 1e). With such MNPs, the previously considered doses are practically ineffective, and one order of magnitude larger quantities should be used to obtain temperature values comparable to the ones reached with FeO@citrate NPs in Fig. 4. As an example, Fig. 9 shows the results found when a SPIO@dextran dose corresponding to an iron mass concentration [Fe] of 12.5 mg/cm^3 is considered. It is interesting to note that even with this very high dose, with configurations #2 (Fig. 9a), #3 (Fig. 9b) and #4 (Fig. 9c) the therapeutic range is not reached in terms of average temperature when f = 150 kHz, also when a current of 300 A is supplied. On the contrary, with configuration #1 (Fig. 9a), a current of 100 A is sufficient to achieve target thermal conditions.

With 300 kHz it is always possible to overcome the limit of 40 °C and, interestingly, a remarkable variation of the behaviour with respect to the case with f = 150 kHz can be observed, as a consequence of the relative large change of SLP. In this case, attention has to be paid when using large currents due to the possibility of exceeding the limit of 45 °C, not only locally, but also in terms of average values, as happens for configuration #1 (Fig. 9a), when $\hat{I}$ = 150 A.

In summary, the FeO@citrate NPs offer the best thermal efficiency and safest treatment conditions, since they enable the attainment of therapeutic temperatures with minimal doses and low magnetic field amplitudes, for both the considered frequencies. In particular, with such MNPs effective magnetic hyperthermia application is achieved, once carefully selected the supplying parameters, with all the types of applicator-mouse configurations here considered.

4.3. Advancements, limitations and future directions

The numerical methodology here implemented has demonstrated to be a valid tool for addressing the selection of MNP type and operating conditions to be used in magnetic hyperthermia preclinical tests, also thanks to the adoption of computational phantoms with realistic anatomical details. The reliability of our modelling approach is

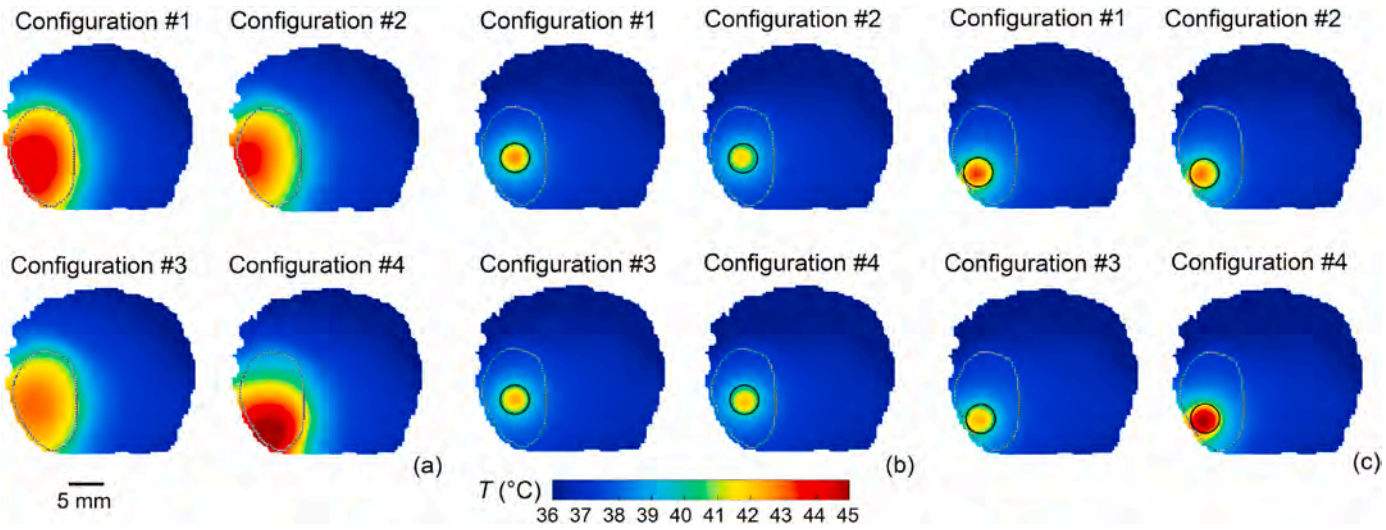

Fig. 7. Analysis of thermal effects due to FeO@citrate (JHU) NP activation for all the considered configurations. Temperature map on a transversal section of the mouse crossing the tumour barycentre, calculated supplying the applicator in configuration #1 with a current of 100 A and the applicators in the other configurations with a current of 300 A, and fixing f to 150 kHz. Different spatial distributions of FeO@citrate NPs are considered: (a) uniform distribution inside the whole tumour with [Fe] = 2 mg/cm^3; (b) uniform distribution in a 4 mm diameter sphere centred in the tumour barycentre, with [Fe] = 10 mg/cm^3; (c) uniform distribution in a 4 mm diameter sphere, located in the tumour and centred at about 2.6 mm from the skin, with [Fe] = 10 mg/cm^3. The spherical regions where the MNPs are dispersed are indicated with a black circle.

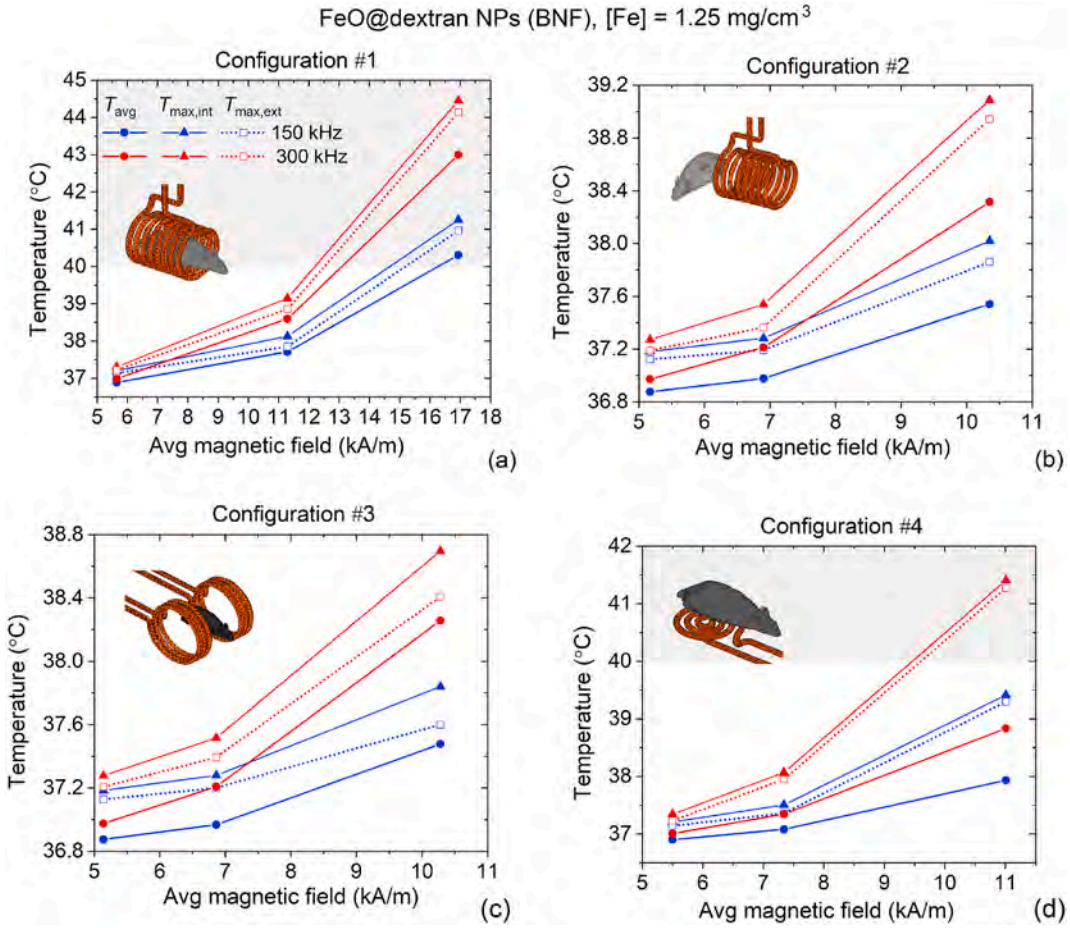

Fig. 8. Analysis of thermal effects due to FeO@dextran (BNF) NP activation for (a) configuration #1, (b) configuration #2, (c) configuration #3, and (d) configuration #4. The graphs show the maximum and average temperatures evaluated at thermal equilibrium within the tumour as a function of the average magnetic field in the tumour, for f equal to 150 kHz and 300 kHz (the maximum temperature external to the body is also reported). The dose of the FeO@dextran NPs, assumed to be uniformly distributed within the tumour, corresponds to an iron mass concentration [Fe] of 1.25 mg/cm^3. The target temperature range for T_{avg} (40−45 °C) is indicated with the grey rectangle.

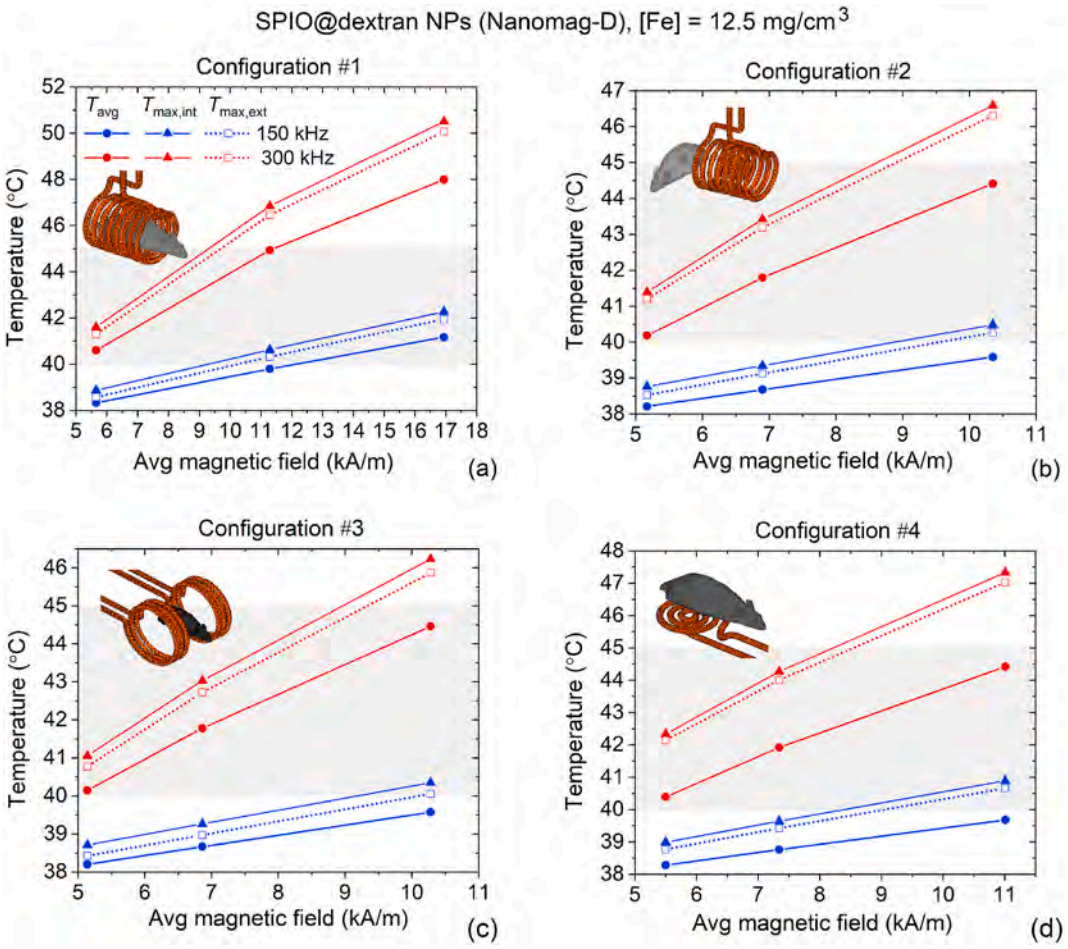

Fig. 9. Analysis of thermal effects due to SPIO@dextran (Nanomag-D) NP activation for (a) configuration #1, (b) configuration #2, (c) configuration #3, and (d) configuration #4. The graphs show the maximum and average temperatures evaluated at thermal equilibrium within the tumour as a function of the average magnetic field in the tumour, for f equal to 150 kHz and 300 kHz (the maximum temperature external to the body is also reported). The dose of the SPIO@dextran NPs, assumed to be uniformly distributed within the tumour, corresponds to an iron mass concentration [Fe] of 12.5 mg/cm^3. The target temperature range for T_{avg} (40–45 °C) is indicated with the grey rectangle.

confirmed by the good agreement between calculated and experimental results, when analogous treatment conditions are considered. As an example, the temperature increase obtained for the FeO@citrate NPs with configuration #3 is comparable to the one measured during *in vivo* tests on mice with the same tumour volume, when using a similar applicator and MNPs with SLP values and concentrations that lead to a similar specific heating power in the target region [55].

Our modelling approach can be easily extended to simulate human applications in view of a treatment plan design, as envisaged in previous works, where *in silico* tests of breast, head and pancreas tumour treatment were performed [56–58]. An advantage of our methodology is the possibility of including in the bioheat simulations the dependence of the MNP heating properties on the local values of the magnetic field, introducing a spatially-dependent heating power of the MNPs, while in most of the studies the field is supposed to be uniform in the target region where the MNPs are dispersed. This enables us to investigate the influence of the coil geometry and position with respect to the anatomical target region, providing indications for the design and proper placement of the field applicator, also for deep-seated tumours. Moreover, thanks to our approach, it is possible to evaluate the overall temperature increase in tissues, adding to the contribution of MNPs the undesired heating effects associated with eddy current generation. In this way, we can guide the design of field applicators and protocols that fulfil biophysical requirements, reducing risks for safety and non-selective heating of healthy tissues, which are more likely to occur when the body part exposed to the field is large, as for human adult thorax.

As a limitation of our methodology, thermoregulation or temperature-dependence of blood perfusion phenomena are not currently taken into account [59]. Moreover, the reliability of the model resides in the quality of estimation of the tissue thermal properties, whose accurate characterization is a very complex task, also considering that they are typically derived from *ex vivo* measurements. One main issue is the lack of enough experimental data on tumour region properties, also considering the complex perfusion patterns arising in tumours. In our modelling approach, we refer to data retrieved from the literature, as commonly done. Obviously, different thermal properties lead to a different thermal response, with implications on the definition of efficacious and safe treatment plans. Anyway, a combined variation of 20% in the most impactful tumour parameters (electrical conductivity, thermal conductivity and tissue-blood perfusion rate) is demonstrated to lead to a maximum variation in the local temperature of about 0.8 °C, as shown in the sensitivity analysis reported in the Supplemental Material (Table S2).

Another criticality regards the proper knowledge of the MNP SLP, which depends on many factors, including the excitation conditions (peak amplitude and frequency of the AC magnetic field), the MNP properties (size, shape, material composition, surface coating, and aggregation state) [60–62], and the viscosity of the medium where they are dispersed. It is worth noting that experimental SLP values used in

this work were derived from measurements in water, thus including possible Brownian rotation effects that can be appreciable in low viscosity media, depending on the MNP size [63]. On the contrary, these effects are typically suppressed when MNPs are confined within tissues, translating in eventually lower SLP values and thus lower relative increments in temperature. The discrepancy between water and high-viscosity media is difficult to be quantified, being Brownian rotation effects strongly dependent on the MNP size and shape. Moreover, it is important to observe that the derivation of SLP from thermometric and calorimetric measurements can suffer from uncertainties and errors imposed by experimental conditions and estimation methodology [64], thus limiting SLP value reproducibility and reliable use *in silico* tests.

Additionally, more precise simulations for treatment planning require an accurate determination of the spatial distribution of the MNPs in the tumour, which can be affected by the tumour shape and size, the tissue heterogeneity, the rate of infusion of the MNPs, and the number and sites of injections. As a future direction for improving the realism of *in silico* tests, the bioheat simulations can be combined with modelling approaches able to predict MNP concentration profile during the infusion [65] or with microCT image based simulations [66]. As a further step, heterogeneity in tumour composition can be considered, introducing necrotic area, where the rate of MNP penetration drops drastically [67], as well as spatially varying blood perfusion properties [68].

Finally, thanks to the possibility of simulating the entire treatment pipeline, from the field applicator design to the evaluation of the temperature increase, another step forward of our methodology can be the optimization of the applicator coils. In this direction, the objective is the engineering of applicators with proper electronic circuit, able to generate AC magnetic fields with amplitudes suitable for magnetic hyperthermia and treatment of non-superficial tumours, too. As a requirement, low supply currents (less than 100 A) should be used, to reduce the risks of conductor overheating as much as possible. To this aim, our modelling approach could be further extended to include Joule loss effects within the coil wires and heat transfer from the conductors to the surrounding environment, also for supporting the design of applicator cooling systems [69].

5. Conclusions

In this study, we have simulated magnetic hyperthermia *in vivo* tests to investigate the thermal response in a mouse, produced by AC magnetic field exposure and consequent MNP activation, under realistic operative conditions. The obtained results have shown that the treatment outcomes, in terms of temperature increments in the target region, can strongly depend not only on the amplitude and frequency of the local magnetic field, but also on its spatial distribution, which varies with the geometry of the applicator and its position with respect to the body. Therefore, a detailed knowledge of these information, besides MNP heating properties, is essential for optimizing the tumour exposure to the AC magnetic field and thus planning an effective and safe treatment. When the animal is positioned within the wires of helical or Helmholtz coils, strongly uniform fields can be generated inside the body, with larger amplitudes observable for the helical coil, thus allowing the use of lower currents and the reduction in technical issues connected to the design of proper power electronics. When the animal is not placed inside the wires, as for helical and pancake coils positioned in close proximity to the tumour, the magnetic field rapidly decays with the distance from the applicator, thus requiring the use of high currents. In this case, a strongly heterogeneous spatial distribution of the field is found, especially for the pancake coil, making the above solutions not suitable for the treatment of deep-seated or very large superficial tumours.

Another important aspect highlighted in our analysis is the need of monitoring the temperature increase during AC magnetic field application to avoid the overheating of healthy tissues. Such effects can appear also in body areas distant from the target region, as happens for the configuration with the mouse placed inside the Helmholtz coil, for which the field exposure is responsible for the generation of eddy currents that circulate from tail to head. In the presence of MNPs uniformly distributed within the tumour, important side effects in the areas surrounding the tumour can appear with all configurations, suggesting to opt for a more localized MNP dosage.

Finally, our study has quantified the thermal response of different MNPs as a function of magnetic field application configuration and supply conditions. When using MNPs like the FeO@citrate (JHU) ones, characterized by relative high values of SLP at low magnetic field amplitudes and frequencies, the temperature therapeutic range can be reached with low doses (in the range of 1 mg/cm^3) and no restrictions need to be imposed on the applicator choice. With less efficient MNPs, like the FeO@dextran (BNF) and SPIO@dextran (Nanomag-D) ones, careful attention has to be paid when selecting the experimental setup, since for certain configurations (e.g., the helical coil with the mouse outside and the Helmholtz coil), sufficiently high temperature increments can be obtained only when using one order of magnitude larger doses.

CRediT authorship contribution statement

Marta Vicentini: Writing – review & editing, Writing – original draft, Visualization, Methodology, Investigation, Formal analysis, Data curation, Software. **Riccardo Ferrero:** Writing – review & editing, Visualization, Investigation, Data curation. **Alessandra Manzin:** Writing – review & editing, Writing – original draft, Visualization, Supervision, Software, Methodology, Investigation, Formal analysis, Data curation, Conceptualization.

Declaration of Competing interest

All authors declare that there are not any financial and personal relationships with other people or organisations that could inappropriately influence (bias) their work.

Data availability

Data will be made available on request.

Appendix A. Supplementary data

Supplementary data to this article can be found online at https://doi.org/10.1016/j.ijthermalsci.2024.109151.

References

[1] X. Liu, et al., Comprehensive understanding of magnetic hyperthermia for improving antitumor therapeutic efficacy, Theranostics 10 (8) (2020) 3793–3815.
[2] Q.A. Pankhurst, J. Connolly, S.K. Jones, J. Dobson, Applications of magnetic nanoparticles in biomedicine, J. Phys. D Appl. Phys. 36 (13) (2003) R167–R181.
[3] D. Chang, M. Lim, J.A.C.M. Goos, R. Qiao, Y. Yee Ng, F.M. Mansfeld, M. Jackson, T. P. Davis, M. Kavallaris, Biologically targeted magnetic hyperthermia: potential and limitations, Front. Pharmacol. 9 (2018) 831.
[4] H.F. Rodrigues, G. Capistrano, A.F. Bakuzis, In vivo magnetic nanoparticle hyperthermia: a review on preclinical studies, low-field nano-heaters, noninvasive thermometry and computer simulations for treatment planning, Int. J. Hyperther. 37 (3) (2020) 76–99.
[5] V. Vilas-Boas, F. Carvalho, B. Espiña, Magnetic hyperthermia for cancer treatment: main parameters affecting the outcome of in vitro and in vivo studies, Molecules 25 (12) (2020) 2874.
[6] A.-R. Tsiapla, A.-A. Kalimeri, N. Maniotis, E. Myrovali, T. Samaras, M. Angelakeris, O. Kalogirou, Mitigation of magnetic particle hyperthermia side effects by magnetic field controls. International Journal of hyperthermia: the Official Journal of European Society for hyperthermic Oncology, north American hyperthermia group, Int. J. Hyperther. 38 (1) (2021) 511–522.
[7] W.J. Atkinson, I.A. Brezovich, D.P. Chakraborty, Useable frequencies in hyperthermia with thermal seeds, IEEE Trans. Biomed. Eng. 31 (1) (1984) 70–75.
[8] L. Bubnovskaya, A. Belous, S. Solopan, A. Kovelskaya, L. Bovkun, A. Podoltsev, I. Kondtratenko, S. Osinsky, Magnetic fluid hyperthermia of rodent tumors using manganese perovskite nanoparticles, Journal of Nanoparticles 2014 (2014) 278761.

[9] M. Johannsen, et al., Magnetic fluid hyperthermia (MFH) reduces prostate cancer growth in the orthotopic Dunning R3327 rat model, Prostate 64 (3) (2005) 283–292.

[10] F. Oltolina, A. Peigneux, D. Colangelo, N. Clemente, A. D'Urso, G. Valente, G. R. Iglesias, C. Jimenez-Lopez, M. Prat, Biomimetic magnetite nanoparticles as targeted drug nanocarriers and mediators of hyperthermia in an experimental cancer model, Cancers 12 (9) (2020) 2564.

[11] T.J. Carter, et al., Potential of magnetic hyperthermia to stimulate localized immune activation, Small 17 (14) (2021) 2005241.

[12] W. Lin, X. Xie, Y. Yang, X. Fu, H. Liu, Y. Yang, J. Deng, Thermosensitive magnetic liposomes with doxorubicin cell-penetrating peptides conjugate for enhanced and targeted cancer therapy, Drug Deliv. 23 (9) (2016) 3436–3443.

[13] S. Kossatz, et al., Efficient treatment of breast cancer xenografts with multifunctionalized iron oxide nanoparticles combining magnetic hyperthermia and anti-cancer drug delivery, Breast Cancer Res. 17 (1) (2015) 66.

[14] S. Piehler, et al., Iron oxide nanoparticles as carriers for DOX and magnetic hyperthermia after intratumoral application into breast cancer in mice: impact and future perspectives, Nanomaterials 10 (6) (2020) 1016.

[15] A. Espinosa, et al., Magnetic (hyper)thermia or photothermia? Progressive comparison of iron oxide and gold nanoparticles heating in water, in cells, and in vivo, Adv. Funct. Mater. 28 (37) (2018) 1803660.

[16] A.P. Sangnier, S. Preveral, A. Curcio, A.K.A. Silva, C.T. Lefèvre, D. Pignol, Y. Lalatonne, C. Wilhelm, Targeted thermal therapy with genetically engineered magnetite magnetosomes@RGD: photothermia is far more efficient than magnetic hyperthermia, J. Contr. Release 279 (2018) 271–281.

[17] A. Curcio, A.K.A. Silva, S. Cabana, A. Espinosa, B. Baptiste, N. Menguy, C. Wilhelm, A. Abou-Hassan, Iron oxide nanoflowers@CuS hybrids for cancer tri-therapy: interplay of photothermal therapy, magnetic hyperthermia and photodynamic therapy", Theranostics 9 (5) (2019) 1288–1302.

[18] Z.-Q. Zhang, S.-C. Song, Thermosensitive/superparamagnetic iron oxide nanoparticle-loaded nanocapsule hydrogels for multiple cancer hyperthermia, Biomaterials 106 (2016) 13–23.

[19] O. Sandre, C. Genevois, E. Garaio, L. Adumeau, S. Mornet, F. Couillaud, In vivo imaging of local gene expression induced by magnetic hyperthermia, Genes 8 (2) (2017) 61.

[20] N.A. Brusentsov, L.V. Nikitin, T.N. Brusentsova, A.A. Kuznetsov, F.S. Bayburtskiy, L.I. Shumakov, N.Y. Jurchenko, Magnetic fluid hyperthermia of the mouse experimental tumor, J. Magn. Magn Mater. 252 (2002) 378–380.

[21] C.L. Dennis, A.J. Jackson, J.A. Borchers, P.J. Hoopes, R. Strawbridge, A. R. Foreman, J. van Lierop, C. Grüttner, R. Ivkov, Nearly complete regression of tumors via collective behavior of magnetic nanoparticles in hyperthermia, Nanotechnology 20 (39) (2009) 395103.

[22] X. Ma, et al., Fe_3O_4–Pd Janus nanoparticles with amplified dual-mode hyperthermia and enhanced ROS generation for breast cancer treatment, Nanoscale Horiz 4 (6) (2019) 1450–1459.

[23] H.A. Albarqi, A.A. Dermessie, F.Y. Sabei, A.S. Moses, M.N. Hansen, P. Dhagat, O. R. Taratula, O. Taratula, Systemically delivered magnetic hyperthermia for prostate cancer treatment, Pharmaceutics 12 (11) (2020) 1020.

[24] X.L. Liu, et al., Synthesis of ferromagnetic $Fe_{0.6}Mn_{0.4}O$ nanoflowers as a new class of magnetic theranostic platform for in vivo T_1-T_2 dual-mode magnetic resonance imaging and magnetic hyperthermia therapy, Adv. Healthcare Mater. 5 (16) (2016) 2092–2104.

[25] J. Lee, et al., Exchange-coupled magnetic nanoparticles for efficient heat induction, Nat. Nanotechnol. 6 (2011) 418–422.

[26] O.K. Arriortua, et al., Antitumor magnetic hyperthermia induced by RGD-functionalized Fe_3O_4 nanoparticles, in an experimental model of colorectal liver metastases, Beilstein J. Nanotechnol. 7 (2016) 1532–1542.

[27] R. Hergt, S. Dutz, Magnetic particle hyperthermia - biophysical limitations of a visionary tumour therapy, J. Magn. Magn Mater. 311 (1) (2007) 187–192.

[28] M. Vicentini, M. Vassallo, R. Ferrero, I. Androulakis, A. Manzin, In silico evaluation of adverse eddy current effects in preclinical tests of magnetic hyperthermia, Comput. Methods Progr. Biomed. 223 (2022) 106975.

[29] R.R. Wildeboer, P. Southern, Q.A. Pankhurst, On the reliable measurement of specific absorption rates and intrinsic loss parameters in magnetic hyperthermia materials, J. Phys. D Appl. Phys. 47 (2014) 495003.

[30] R. Ferrero, G. Barrera, F. Celegato, M. Vicentini, H. Sözeri, N. Yıldız, C.A. Dinçer, M. Coïsson, A. Manzin, P. Tiberto, Experimental and modelling analysis of the hyperthermia properties of iron oxide nanocubes, Nanomaterials 11 (9) (2021) 2179.

[31] M. Cobianchi, A. Guerrini, M. Avolio, C. Innocenti, M. Corti, P. Arosio, F. Orsini, C. Sangregorio, A. Lascialfari, Experimental determination of the frequency and field dependence of specific loss power in magnetic fluid hyperthermia, J. Magn. Magn Mater. 444 (2017) 154–160.

[32] N.N. Liu, A.P. Pyatakov, A.M. Saletsky, M.N. Zharkov, N.A. Pyataev, G. B. Sukhorukov, Y.K. Gun'ko, A.M. Tishin, The "field or frequency" dilemma in magnetic hyperthermia: the case of Zn–Mn ferrite nanoparticles, J. Magn. Magn Mater. 555 (2022) 169379.

[33] F. Soetaert, S.K. Kandala, A. Bakuzis, R. Ivkov, Experimental estimation and analysis of variance of the measured loss power of magnetic nanoparticles, Sci. Rep. 7 (2017) 6661.

[34] M. Vassallo, et al., Improvement of hyperthermia properties of iron oxide nanoparticles by surface coating, ACS Omega 8 (2) (2023) 2143–2154.

[35] M. Vicentini, R. Ferrero, A. Manzin, In silico experiments to explore the heating efficiency of magnetic nanoparticles in hyperthermia preclinical tests, Adv. Theory Simul. 6 (7) (2023) 2300234.

[36] M. Ohtake, et al., Hyperthermia and chemotherapy using Fe(Salen) nanoparticles might impact glioblastoma treatment, Sci. Rep. 7 (2017) 42783.

[37] H.F. Rodrigues, G. Capistrano, F.M. Mello, N. Zufelato, E.P. Silvera-Lacerda, A. F. Bakuzis, Precise determination of the heat delivery during in vivo magnetic nanoparticle hyperthermia with infrared thermography, Phys. Med. Biol. 62 (10) (2017) 4062–4082.

[38] H.F. Rodrigues, F.M. Mello, L.C. Branquinho, N. Zufelato, E.P. Silvera-Lacerda, A. F. Bakuzis, Real-time infrared thermography detection of magnetic nanoparticle hyperthermia in a murine model under a non-uniform field configuration, Int. J. Hyperther. 29 (8) (2013) 752–767.

[39] T. Araya, K. Kasahara, S. Nishikawa, H. Kimura, T. Sone, H. Nagae, Y. Ikehata, I. Nagano, M. Fujimura, Antitumor effects of inductive hyperthermia using magnetic ferucarbotran nanoparticles on human lung cancer xenografts in nude mice, OncoTargets Ther. 6 (2013) 237–242.

[40] Y. Hadadian, M. Azimbagirad, E.A. Navas, T.Z. Pavan, A versatile induction heating system for magnetic hyperthermia studies under different experimental conditions, Rev. Sci. Instrum. 90 (7) (2019) 074701.

[41] M.E. Cano, A. Barrera, J.C. Estrada, A. Hernandez, T. Cordova, An induction heater device for studies of magnetic hyperthermia and specific absorption ratio measurements, Rev. Sci. Instrum. 82 (11) (2011) 114904.

[42] M. Zeinoun, D. Serrano, P. Tezanos Medina, O. García, M. Vasić, J.J. Serrano-Olmedo, Configurable high-frequency alternating magnetic field generator for nanomedical magnetic hyperthermia applications, IEEE Access 9 (2021) 105805–105816.

[43] L. Souiade, J. Domingo-Diez, C. Alcaide, B. Gámez, L. Gámez, M. Ramos, J. J. Serrano Olmedo, Int. J. Mol. Sci. 24 (2023) 15933.

[44] E.A. Périgo, G. Hemery, O. Sandre, D. Ortega, E. Garaio, F. Plazaola, F.J. Teran, Fundamentals and advances in magnetic hyperthermia, Appl. Phys. Rev. 2 (2015) 041302.

[45] A. Manzin, R. Ferrero, M. Vicentini, From micromagnetic to in silico modeling of magnetic nanodisks for hyperthermia applications, Adv. Theory Simul. 4 (5) (2021) 2100013.

[46] H. Corte-León, V. Neu, A. Manzin, C. Barton, Y. Tang, M. Gerken, P. Klapetek, H. W. Schumacher, O. Kazakova, Comparison and validation of different magnetic force microscopy calibration schemes, Small 16 (11) (2020) 1906144.

[47] R. Scorretti, N. Burais, O. Fabregue, A. Nicolas, L. Nicolas, Computation of the induced current density into the human body due to relative LF magnetic field generated by realistic devices, IEEE Trans. Magn. 40 (2) (2004) 643–646.

[48] IT'IS Foundation, Animal Models, https://itis.swiss/virtual-population/animal-models/animals/(accessed: December 2023)..

[49] IT'IS Foundation, Tissue Properties, https://itis.swiss/virtual-population/tissue-properties/overview/(accessed: December 2023). .

[50] A. Trakic, F. Liu, S. Crozier, Transient temperature rise in a mouse due to low-frequency regional hyperthermia, Phys. Med. Biol. 51 (7) (2006) 1673–1691.

[51] A. Attaluri, et al., Magnetic nanoparticle hyperthermia enhances radiation therapy: a study in mouse models of human prostate cancer, Int. J. Hyperther. 31 (4) (2015) 359–374.

[52] R.V. Stigliano, F. Shubitidze, A.A. Petryk, J.A. Tate, P.J. Hoopesa, Magnetic nanoparticle hyperthermia: predictive model for temperature distribution, Proc. SPIE-Int. Soc. Opt. Eng. 8584 (2013) 858410.

[53] M. Wabler, W. Zhu, M. Hedayati, A. Attaluri, H. Zhou, J. Mihalic, A. Geyh, T. L. DeWeese, R. Ivkov, D. Artemov, Magnetic resonance imaging contrast of iron oxide nanoparticles developed for hyperthermia is dominated by iron content, Int. J. Hyperther. 30 (3) (2014) 192–200.

[54] C.L. Dennis, et al., Internal magnetic structure of nanoparticles dominates time-dependent relaxation processes in a magnetic field, Adv. Funct. Mater. 25 (27) (2015) 4300–4311.

[55] G. Capistrano, H.F. Rodrigues, N. Zufelato, C. Gonçalves, C.G. Cardoso, E. P. Silveira-Lacerda, A.F. Bakuzis, Noninvasive intratumoral thermal dose determination during in vivo magnetic nanoparticle hyperthermia: combining surface temperature measurements and computer simulations, Int. J. Hyperther. 37 (3) (2020) 120–140.

[56] R. Rahpeima, C.-A. Lin, Numerical study of magnetic hyperthermia ablation of breast tumor on an anatomically realistic breast phantom, PLoS One 17 (9) (2022) e0274801.

[57] G. Bellizzi, O.M. Bucci, G. Chirico, Numerical assessment of a criterion for the optimal choice of the operative conditions in magnetic nanoparticle hyperthermia on a realistic model of the human head, Int. J. Hyperther. 32 (6) (2016) 688–703.

[58] L. Shoshiashvili, I. Shamatava, D. Kakulia, F. Shubitidze, Design and assessment of a novel biconical human-sized alternating magnetic field coil for MNP hyperthermia treatment of deep-seated cancer, Cancers 15 (2023) 1672.

[59] B. Erdmann, J. Lang, M. Seebass, Optimization of temperature distributions for regional hyperthermia based on a nonlinear heat transfer model, Ann. N. Y. Acad. Sci. 858 (1) (1998) 36–46.

[60] R. Ferrero, M. Vicentini, A. Manzin, Influence of size, volume concentration and aggregation state on magnetic nanoparticle hyperthermia properties versus excitation conditions, Nanoscale Adv. 6 (2024) 1739–1749.

[61] H. Gavilán, K. Simeonidis, E. Myrovali, E. Mazarío, O. Chubykalo-Fesenko, R. Chantrell, Ll Balcells, M. Angelakeris, M.P. Morales, D. Serantes, How size, shape and assembly of magnetic nanoparticles give rise to different hyperthermia scenarios, Nanoscale 13 (2021) 15631–15646.

[62] R. Ferrero, A. Manzin, G. Barrera, F. Celegato, M. Coïsson, P. Tiberto, Influence of shape, size and magnetostatic interactions on the hyperthermia properties of permalloy nanostructures, Sci. Rep. 9 (2019) 6591.

[63] M. Avolio, A. Guerrini, F. Brero, C. Innocenti, C. Sangregorio, M. Cobianchi, M. Mariani, F. Orsini, P. Arosio, A. Lascialfari, In-gel study of the effect of magnetic

nanoparticles immobilization on their heating efficiency for application in Magnetic Fluid Hyperthermia, J. Magn. Magn Mater. 471 (2019) 504–512.
[64] A. Makridis, S. Curto, G.C. van Rhoon, T. Samaras, M. Angelakeris, A standardisation protocol for accurate evaluation of specific loss power in magnetic hyperthermia, J. Phys. D Appl. Phys. 52 (2019) 255001.
[65] F. Di Michele, G. Pizzichelli, B. Mazzolai, E. Sinibaldi, On the preliminary design of hyperthermia treatments based on infusion and heating of magnetic nanofluids, Math. Biosci. 262 (2015) 105–116.
[66] A. LeBrun, R. Ma, L. Zhu, MicroCT image based simulation to design heating protocols in magnetic nanoparticle hyperthermia for cancer treatment, J. Therm. Biol. 62 (2016) 129–137.
[67] M. Sefidgar, E. Bashooki, P. Shojaee, Numerical simulation of the effect of necrosis area in systemic delivery of magnetic nanoparticles in hyperthermia cancer treatment, J. Therm. Biol. 94 (2020) 102742.
[68] M. Singh, Modified Pennes bioheat equation with heterogeneous blood perfusion: a newer perspective, Int. J. Heat Mass Tran. 218 (2024) 124698.
[69] P. Gas, Behavior of helical coil with water cooling channel and temperature dependent conductivity of copper winding used for MFH purpose, IOP Conf. Ser. Earth Environ. Sci. 214 (2019) 012124.